machines

MDPI

Article

Modelling and Stability Analysis for a Magnetically Levitated Slice Motor (MLSM) with Gyroscopic Effect and Non-Collocated Structure Based on the Extended Inverse Nyquist Stability Criterion

Lingling Li, Yang Yu, Liang Hu *, Xiaodong Ruan, Rui Su and Xin Fu

State Key Laboratory of Fluid Power and Mechatronic Systems, Zhejiang University, Hangzhou 310027, China; linglingli@zju.edu.cn (L.L.); 21925076@zju.edu.cn (Y.Y.); xdruan@zju.edu.cn (X.R.); srhello@zju.edu.cn (R.S.); xfu@zju.edu.cn (X.F.)

* Correspondence: cmeehuli@zju.edu.cn; Tel.: +86-135-7578-4077

Abstract: Stability of the rotor motion is the precondition for the reliable operation of magnetically levitated slice motors (MLSMs). However, with gyroscopic effect and non-collocated structure existing simultaneously, its stability analysis faces a tremendous challenge, because the torsional motions couple with the radial translational ones, making MLSM a multiple-input and multiple-output (MIMO) system with high order. Therefore, in this paper, we first establish a novel MIMO rotor dynamics closed-loop model and further convert it into an equivalent single-input and single-out (SISO) feedback control system by constructing complex variables, meanwhile reducing the system order by half. Beneficial from the equivalence between the MIMO and SISO systems, the sufficient and necessary conditions of the absolute stability of MLSM are derived by the extended inverse Nyquist stability criterion in the complex domain. Additionally, the effectiveness of the proposed modelling and stability analysis method is evaluated by simulation and experimental results. Thus, apart from PID parameters, this paper demonstrates that the stability of MLSM is also affected by the coupling of gyroscopic effect and non-collocated structure, which should serve as an essential guideline for system regulation of MLSM.

Keywords: magnetically levitated slice motor; gyroscopic effect; non-collocated structure; equivalent SISO feedback control system; extended inverse Nyquist stability criterion

Citation: Li, L.; Yu, Y.; Hu, L.; Ruan, X.; Su, R.; Fu, X. Modelling and Stability Analysis for a Magnetically Levitated Slice Motor (MLSM) with Gyroscopic Effect and Non-Collocated Structure Based on the Extended Inverse Nyquist Stability Criterion. *Machines* **2021**, *9*, 201. https://doi.org/10.3390/machines9090201

Academic Editor: Alejandro Gómez Yepes

Received: 9 August 2021
Accepted: 17 September 2021
Published: 18 September 2021

1. Introduction

In recent years, there have been increasing demands for ultrapure and miniature systems in many advanced industrial fields, such as the pharmaceutical, biotechnological, chemical, and semiconductor industries [1–4]. With all the degrees of freedom of the rotor actively controlled or passively positioned by the magnetic field, a magnetically levitated slice motor (MLSM) can operate with no abrasion and no contamination due to its non-contacting and non-lubricating features. Furthermore, because of the improved compactness, simpler structure and lower cost, the MLSM is superior to magnetic bearings in the industrial applications mentioned above [5,6].

Nevertheless, the development and further application of MLSMs are hindered due to the following features: (i) the simplified mechanical structure is at the cost of much stronger interaction in the magnetic domain [7]; (ii) a large inertia ratio of the rotor facilitates higher stiffness of passive suspension but meanwhile leads to a significant gyroscopic effect, characterized by precession and nutation modes at high speed [8–11]; (iii) the interference between actively controlled translational directions and passively stabilized tilting directions is inevitable [12] when a non-collocated structure exists, as can be seen in various centrifugal pumps [2,4,13,14]. Sugimoto et al. defined and explained the non-collocated structure concept thoroughly in [15]. To sum up, many factors may destabilize

the rotor in a MLSM, which leads to collisions and produces particles in the MLSM-based system. Therefore, MLSM is such a complicated system that it is challenging to analyze its stability parameters for better controllability, especially when the gyroscopic effect and non-collocated structure exist simultaneously.

In the last decades, researches on the operating stability of magnetically suspended rigid flat rotors have attracted widespread attention, since this type of rotor possesses outstanding advantages, including high power density, high efficiency and small volume [16,17]. Over the whole range of spin speeds, Fang et al. employed positive and negative frequency characteristics to analytically demonstrate the nutation and precession stability criteria for a magnetically suspended rigid rotor system with cross-feedback control [18]. Wei et al. presented an absolute and relative stability analysis for magnetically suspended rigid rotors in the frequency domain by analyzing the corresponding Nyquist curves, and furtherly proposed a method to calculate the stable rotation speed region [19]. Regarding asymmetric rotors, Sun et al. utilized the double-frequency Bode plot method to judge the instability caused by nutation mode and designed the exact parameters of filter cross feedback accordingly [10]. However, all the stability criteria mentioned above are limited to rotors suspended by magnetic bearings, and hence not suitable for rotors in MLSMs. In case of single-drive bearingless motor, the interference coefficients of tilting torque and radial force relative to axial position of the center of gravity of the rotor were calculated by 3D-FEM analysis [20]. Based on experiments in [21], Sugimoto et al. described how gyroscopic effect influenced the operating condition regarding the system in [20]. Still, neither of them presented sufficient theoretical analysis. From rotational tests on disk-shaped rotors of a multi-pole bearingless machine with a non-collocated structure, it was concluded that tilting and radial translational vibrations tended to occur as a consequence of the mutual interference which was proportional to the rotational speed and axial distance between the active radial suspension force and the center of gravity of the rotor [22]. However, only a qualitative analysis of specific parameters was conducted at rather low rotational speed, so essentially the cause of system instability was not explained and the conclusion had no universal applicability. In [15], a MLSM with a non-collocated structure was represented as a fifth-order system and its stability condition was derived by applying the Hurwitz stability criterion. Nevertheless, the mathematical calculation was too complicated to be used to analyze the suspension stability during rotation due to its much higher system order.

Based on the above analysis on gyroscopic effect and non-collocated structure, it can be concluded that close attention should be paid to both scenarios to ensure the stability of MLSMs. Non-collocated structures received a comprehensive study in [15] and the gyroscopic effect are already individually investigated in many studies on magnetically levitated flat rotors, because it leads to two poles located on the imaginary axis. Hence, this paper intends to provide the way to regulate and sequentially ensure the stability of MLSMs where the gyroscopic effect inevitably interacts with a non-collocated structure. To the best of the authors' knowledge, this paper investigates theoretically and experimentally for the first time how both the coupling of the gyroscopic effect and the non-collocated structure act on the stability of a MLSM. A novel closed-loop model is first set up to simultaneously describe the rotor dynamics of MLSM undergoing gyroscopic effect and with a non-collocated structure, which turns out to be MIMO and coupled. Then, motivated by the outstanding convenience and simplicity of stability analysis with SISO system in classical control theory, we make an effort to convert the derived MIMO model to a SISO one by constructing complex variables. Consequently, benefitting from the extended inverse Nyquist stability criterion, the condition of stability for the targeted MSLM can be deduced. The simulation and experimental results have verified that the rotor motion stability of MLSM varies, when the relations between gyroscopic effect and non-collocated structure get altered.

2. Modelling of MLSM with Gyroscopic Effect and Non-Collocated Structure

2.1. Working Principle of the MLSM

In order to produce bearing force and driving torque in a single motor simultaneously, a set of suspension coils is superposed on the same stator slots besides driving coils in MLSM. Driving coils generate torque as they work in a permanent-magnet synchronous motor. A radial bearing force can be produced if the difference between pole-pair numbers of suspension coils and driving coils is +1 or −1 while currents in these two sets of coils have equal frequency [7,23]. Figure 1 depicts the principle of bearing force generation in detail, where the pole-pair numbers of suspension coils denoted by N_{Bd}, N_{Bq} and driving coils denoted by N_{dd}, N_{dq} are 2 and 1, respectively. In Figure 1a, flux of suspension coils makes flux of driving coils and permanent magnet increased in the right air gap while decreased in the left, which generates bearing force in the x-direction. Similarly, in Figure 1b, the superposition strengthens flux in the upper air gap but weakens flux in the lower part, leading to bearing force in the y-direction. Thus, bearing force can be controlled in arbitrary directions by adjusting the current in suspension coils [24–26]. Summarily, axial rotational and radial translational degrees of freedom are actively controlled by the driving and suspension coils, respectively.

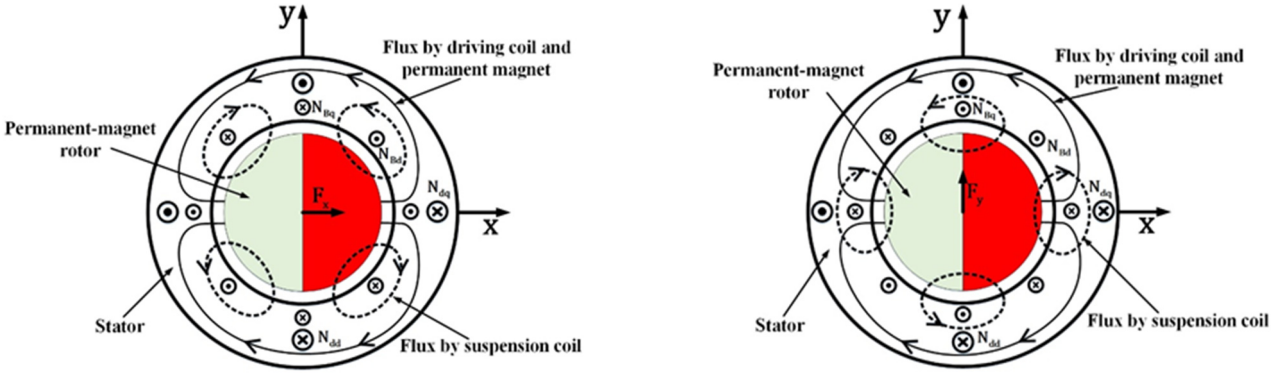

Figure 1. Principle of bearing force generation. (**a**) *x*-direction; (**b**) *y*-direction.

However, different from the aforementioned three degrees of freedom, axial translation and radial tilting are passively positioned. As can be seen in Figure 2a,b, based on the minimum reluctance principle, corresponding restoring force F_{stab} or restoring moment T_{stab} develops to pull the permanent-magnet rotor back to its balanced position when it deflects in axial or tilting direction [27–29].

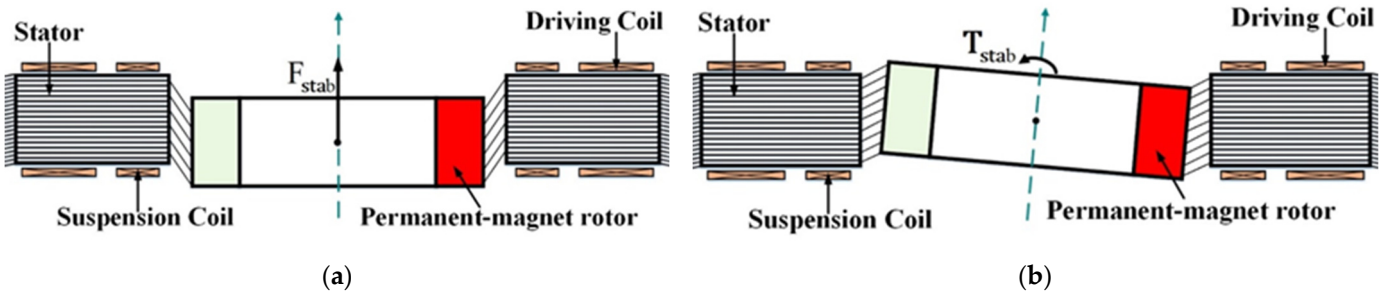

Figure 2. Passive stability. (**a**) axial direction; (**b**) tilting direction.

2.2. Kinetics Analysis of the MLSM System Featured with Gyroscopic Effect

Figure 3 gives the coordinate system definition of the MLSM, where O-xyz is the inertial coordinate system fixed to the stator while N-XYZ is the rotating coordinate system fixed to the rotor. Here, O and N refer to the center of stator and the center of gravity of rotor,

respectively. α, β, γ denote the inclinations of rotor about the *x*-, *y*-, and *z*-axes, respectively. The spin velocity Ω defined by $\Omega = \dot{\gamma}$ is assumed to be constant. In addition, since the rotor has equal moments of inertia in the radial direction because of its symmetrical structure, radial motions are decoupled from the axial rotational one [30]. Meanwhile, considering the following several aspects, the kinetic equation of rotor axial translation is omitted in Equation (1). For one thing, the variation of axial translation has no effect on the measured translational displacement by the sensors. For another, controller generates force in the radial direction according to the deviation signal between the reference position and the above measured one, which doesn't influence the axial direction. Moreover, in the scope of this manuscript, it is supposed that the rotor maintains no-load operation, signifying that it is only subjected to magnetic force and gravity. Hence, the kinetic equation of rotor axial translational motion can be written as $m\ddot{z} = -k_z z - mg$, where k_z is the axial stiffness and *z* defines the axial translational displacement. Therefore, only radial translational and titling motions are researched in this article.

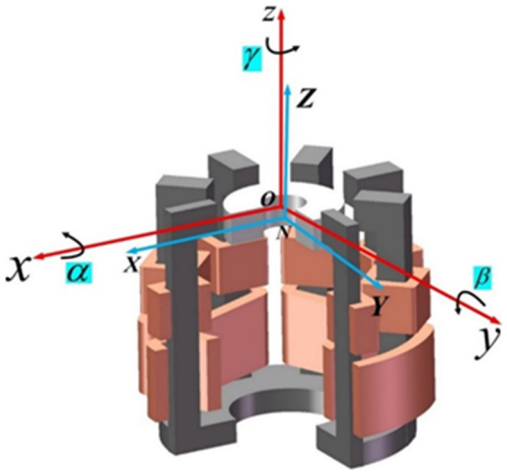

Figure 3. Definition of the coordinate system in MLSM.

x and *y* define the radial translational displacements of N relative to the O-xyz inertial coordinate system. From Lagrange's equations [31], the kinetic equations of rotor radial translational and titling motions can be derived as:

$$\begin{cases} m\ddot{x} = k_x x + F_x + d_x \\ m\ddot{y} = k_y y + F_y + d_y \\ J_X\ddot{\alpha} = -k_\alpha \alpha - J_Z\Omega\,\dot{\beta} + T_\alpha \\ J_Y\ddot{\beta} = -k_\beta \beta + J_Z\Omega\,\dot{\alpha} + T_\beta \end{cases} \quad (1)$$

where m is the mass of the rotor; J_X, J_Y and J_Z are the moments of inertia of the rotor about X-, Y-, and Z-axes, respectively; k_x, k_y and k_α, k_β correspond to the radial and tilting stiffness in *x*- and *y*-directions, respectively. Furthermore, $J_X = J_Y = J$, $k_x = k_y = k_s$ as well as $k_\alpha = k_\beta = k_\theta$. The theoretical formulae of the active radial forces F_x and F_y are consistent with those in the reference [32]. Finally, d_x, d_y, T_α and T_β indicate the total disturbance forces or moments in *x*- and *y*-direction. Here, we set $d_x = d_y = 0$.

2.3. Description of the MLSM with Non-Collocated Structure

Since the non-collocated structure concept has been explained exhaustively in [15], in this section, it is simply reshown only for the description of related parameters. The definitions of each symbol in Figure 4 are as follows: N, S and F represent the center of gravity of rotor, the axial position of radial displacement sensors and the equivalent application point of radial suspension force, respectively. Correspondingly, Z_s and Z_F

denote the axial distance of S and F with respect to N, separately, and their signs are positive above N and negative below N.

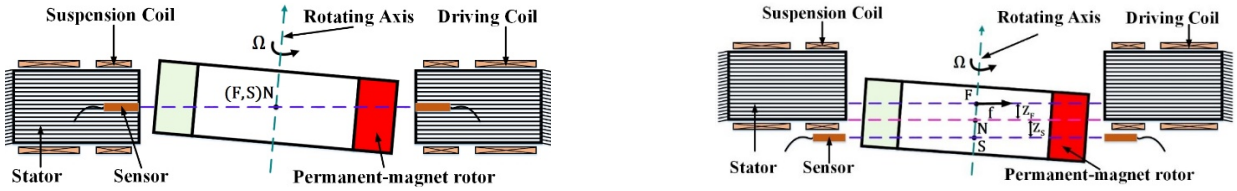

(**a**) (**b**)

Figure 4. Schematic diagram of MLSM with (**a**) collocated structure; (**b**) non-collocated structure.

In order to more intuitively demonstrate how the non-collocated structure affects the torsional stability, Figure 4 shows the case where the rotor possesses an angular displacement around the *x*-axis without any radial translational displacement. Specifically, in Figure 4a, points N, S and F coincide with each other, wherefore there is no extra radial translational displacement detected by the sensors because of the tilting displacement. Consequently, only restoring moment arises from the magnetic resistance, which pulls the rotor back to its balanced position. Under this circumstance, the controllers applied to the radial translational directions have no effect on the tilting ones. However, in Figure 4b, the sensors detect a radial translational displacement at point S due to the tilting motion, which is determined by Z_s and the tilting angle. This radial translational displacement generates a radial force f at point F by the radial feedback controller. Additionally, F is not aligned with N, so a tilting moment produced by f acts in the deflection direction, which destabilizes the tilting motions. It means that tilting movements interfere with radial translational ones in the non-collocated structure. To sum up, the non-collocated structure leads to mutual coupling among degrees of freedom of the rotor movements, so the stability condition of a non-collocated MLSM system should be considered cautiously.

2.4. Analytical Model of the Controlled MLSM System with Gyroscopic Effect and Non-Collocated Structure

With the gyroscopic effect and non-collocated structure taken into account, MLSM under the assumption of no-load operation is characterized by a strongly coupled multiple-input and multiple-output model in Figure 5. To be specific, PID parameters for radial translational motions are designed by following the principles in controller design for one-axis magnetic suspension, which have been illustrated and received extensive applications in the predecessors' research [33]. Subsequently, the gyroscopic effect and non-collocated structure respectively described by $J_Z{*}\Omega$ and Z_S, Z_F are contained to comprehensively reveal the interactions among these four degrees of freedom. It is worth specially mentioning that $Z_S{*}\alpha$, $Z_S{*}\beta$ represent extra radial displacements detected by the sensors due to non-collocated structure, while $Z_F{*}\alpha$, $Z_F{*}\beta$ refer to additional radial forces resulting from non-collocated structure, Besides the effects above, the non-collocated structure also exerts moments on the radial tilting motions, which are evaluated by the products of Z_F and the corresponding resultant radial forces.

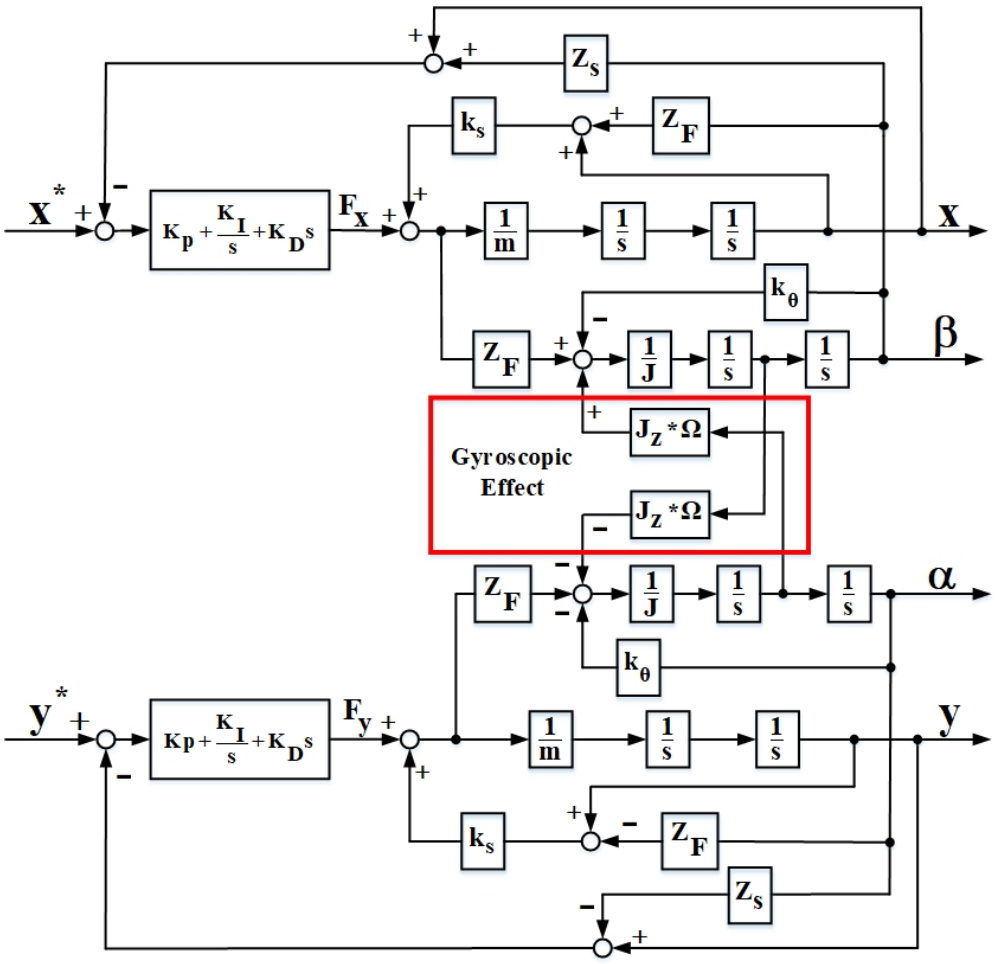

Figure 5. Block diagram of MLSM system considering gyroscopic effect and non-collocated structure.

According to the block diagram in Figure 5, the closed-loop model of MLSM considering gyroscopic effect and non-collocated can be presented in the form below:

$$ms^2x - k_sx + \left(K_p + \frac{K_I}{s} + K_Ds\right)x = \left(K_p + \frac{K_I}{s} + K_Ds\right)x^* + \left[k_sZ_F - \left(K_p + \frac{K_I}{s} + K_Ds\right)Z_s\right]\beta \quad (2)$$

$$ms^2y - k_sy + \left(K_p + \frac{K_I}{s} + K_Ds\right)y = \left(K_p + \frac{K_I}{s} + K_Ds\right)y^* - \left[k_sZ_F - \left(K_p + \frac{K_I}{s} + K_Ds\right)Z_s\right]\alpha \quad (3)$$

$$Js^2\alpha + k_\theta\alpha + \left(K_p + \frac{K_I}{s} + K_Ds\right)Z_sZ_F\alpha - k_sZ_F^2\alpha = -y^*\left(K_p + \frac{K_I}{s} + K_Ds\right)Z_F - \left[k_sZ_F - \left(K_p + \frac{K_I}{s} + K_Ds\right)Z_F\right]y - J_Z\Omega s\beta \quad (4)$$

$$Js^2\beta + k_\theta\beta + \left(K_p + \frac{K_I}{s} + K_Ds\right)Z_sZ_F\beta - k_sZ_F^2\beta = x^*\left(K_p + \frac{K_I}{s} + K_Ds\right)Z_F + \left[k_sZ_F - \left(K_p + \frac{K_I}{s} + K_Ds\right)Z_F\right]x + J_Z\Omega s\alpha \quad (5)$$

where, K_p, K_I and K_D are the proportional, integral and derivative gains, respectively, while meanings of the remaining symbols have been illustrated in detail above. Besides, it is the general situation that both the reference position x^* and y^* are zero.

For the ease of representation and calculation, we make the following substitutions:

$$A = ms^2 - k_s + \left(K_p + \frac{K_I}{s} + K_Ds\right) \quad (6)$$

$$B = k_s Z_F - \left(K_p + \frac{K_I}{s} + K_D s\right) Z_s \tag{7}$$

$$C = Js^2 + k_\theta + \left(K_p + \frac{K_I}{s} + K_D s\right) Z_s Z_F - k_s Z_F^2 \tag{8}$$

$$D = k_s Z_F - \left(K_p + \frac{K_I}{s} + K_D s\right) Z_F \tag{9}$$

Hereafter, Equations (2)–(5) can be presented in a simplified way:

$$x = \frac{B}{A}\beta \tag{10}$$

$$y = -\frac{B}{A}\alpha \tag{11}$$

$$\alpha = -\frac{Dy + J_Z \Omega s \beta}{C} \tag{12}$$

$$\beta = \frac{Dx + J_Z \Omega s \alpha}{C} \tag{13}$$

Because x leads y by 90 degrees in terms of phase and there is the same relationship between α and β likewise, these four variables can be reconstructed by two complex variables, i.e., $X = x + jy$, $\Psi = \alpha + j\beta$, where j represents imaginary unit [34,35]. Performing the basic mathematical operations: $(10) + j(11)$ and $(12) + j(13)$, we can get a new equation set on the complex variables X and Ψ:

$$X = -j\frac{B}{A}\Psi \tag{14}$$

$$\Psi = j\frac{D}{C}X + j\frac{J_Z \Omega s}{C}\Psi \tag{15}$$

Combining (14) with (15) yields:

$$\Psi = \frac{BD}{AC}\Psi + j\frac{J_Z \Omega s}{C}\Psi \tag{16}$$

In order to make the meaning of formula (16) more intuitive, a further mathematical transformation should be given as:

$$AC\Psi = BD\Psi + jAJ_Z \Omega s \Psi \tag{17}$$

Then, substituting $(6) - (9)$ into (17) yields

$$\begin{aligned} &\left[Jms^4 - jmJ_Z \Omega s^3 + \left(mk_\theta - mk_s Z_F^2 - Jk_s\right)s^2 + jJ_Z \Omega k_s s - k_s k_\theta\right]\Psi \\ &= -\left[(J + mZ_s Z_F)s^2 - jJ_Z \Omega s + k_\theta\right]\left(K_p + \tfrac{K_I}{s} + K_D s\right)\Psi \end{aligned} \tag{18}$$

To give prominence to the essence of Equation (18), the following steps are executed: First, a controlled plant as well as the corresponding PID controller is established, whose transfer functions are presented as Equations (19) and (20), respectively. Then, we set up a unit negative feedback system by $G_{contr}(s)$ and $G_{plant}(s)$. Last, respectively setting the input and output of the above system as 0 and Ψ leads to a SISO feedback system as Figure 6, for which the closed-loop transfer function is $\Psi = (0 - \Psi)G_{contr}G_{plant}$. It is easy to derive that Equation (18) equals the result of multiplying both sides of $\Psi = (0 - \Psi)G_{contr}G_{plant}$ by the denominator of Equation (19), where Ψ is a complex variable constructed by $\alpha + j\beta$, as

defined above. In summary, Equation (18) is equivalent to a SISO control system depicted in Figure 6.

$$G_{plant}(s) = \frac{(J + mZ_sZ_F)s^2 - jJ_Z\Omega s + k_\theta}{Jms^4 - jmJ_Z\Omega s^3 + \left(mk_\theta - mk_sZ_F^2 - Jk_s\right)s^2 + jJ_Z\Omega k_s s - k_s k_\theta} \tag{19}$$

$$G_{contr}(s) = K_p + \frac{K_I}{s} + K_D s \tag{20}$$

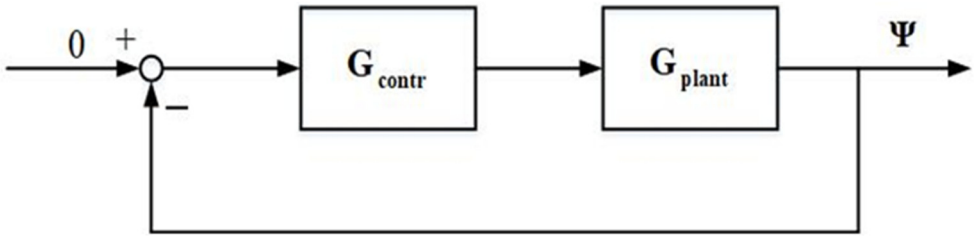

Figure 6. Block diagram of the equivalent SISO control system.

According to the classical control theory, we can write the open-loop transfer function of the system as:

$$G_{OL}(s) = G_{contr}(s)G_{plant}(s) \tag{21}$$

In this section, with the method of variable reconstruction in the complex domain, we transform a two-input four-output coupling system described by (2) − (5) into a SISO one presented by (18). This work can not only greatly reduce the system order, but also make it feasible to apply the extended inverse Nyquist stability criterion of the SISO system to deduce the stability condition for the original MIMO one.

3. Extended Inverse Nyquist Stability Criterion in the Complex Domain

First of all, Cauchy's argument principle is provided [36]: it is supposed that F(s) represents a meromorphic function with P poles and Z zeros circled by C_S which designates a simple closed curve avoiding any zeros and poles of F(s) on S plane. As the point s travels around C_S clockwise, the closed curve C_S is mapped to a closed curve C_F on F plane by F(s), which circles the origin by M times. Finally, we obtain the relationship between the symbols P, Z and M as M = Z − P, where positive M stands for the clockwise encirclements of the origin.

Taking advantage of the property of Cauchy's argument principle, the extended inverse Nyquist stability criterion can be readily summarized in accordance with the classical Nyquist stability criterion proposed by Nyquist [37]:

Theorem 1. *Pertaining to a closed-loop feedback control system containing complex coefficients, the corresponding sufficient and necessary conditions for stability can be described as: the number of times that its open-loop inverse Nyquist plot encloses the point (−1, j0) counterclockwise equals the number of its open-loop zeros located in the right half plane when* $s = j\omega, -\infty < \omega < +\infty$.

Proof of Theorem 1. Without loss of generality, we make G(s)H(s) represent the open-loop transfer function of a common control system. Naturally, a new complex function F(s) can be reformulated with G(s)H(s), as is shown in (22):

$$F(s) = 1 + \frac{1}{G(s)H(s)} \tag{22}$$

The establishment of F(s) can provide a practical and convenient graphical technique for determining the absolute stability of a feedback control system in the light of Cauchy's argument principle. Specifically, the numerator and denominator of F(s) indicate the pole

polynomial of closed-loop transfer function and the zero polynomial of open-loop transfer function, respectively. Besides, polar diagram of $1/G(j\omega)H(j\omega)$ is the so-called inverse Nyquist plot [38–40]. Thereupon, the number of right half-plane poles of the closed-loop system can be calculated from: the number of right half-plane zeros of the open-loop system subtracts the number of times that its open-loop inverse Nyquist plot encloses the point $(-1, j0)$ counterclockwise. Ultimately, the closed-loop system is stable, if and only if the calculation result is zero. □

Remark 1. *As for $1/G(s)H(s)$, the numerator tends to have a higher order compared to its denominator, because $G(s)H(s)$is always real for the open-loop transfer function of a physical system. In such a situation, mapping locus of the clockwise semicircle curve $s = \infty e^{j\theta}$, $\theta \in \left(\frac{\pi}{2}, -\frac{\pi}{2}\right)$has to be considered cautiously. Another point that needs to be taken seriously is that symmetry of the inverse Nyquist curve about the real axis no longer holds for a transfer function with complex coefficients, so there is no way to omit the inverse Nyquist plot in the negative frequency domain. Moreover, given that in the inverse Nyquist plot, the difference between the times of positive and negative crossings about the real axis in the range of $(-\infty, -1)$is identical to the number of encirclements about $(-1, j0)$, we introduce the method to distinguish between different types of crossing in Figure 7.*

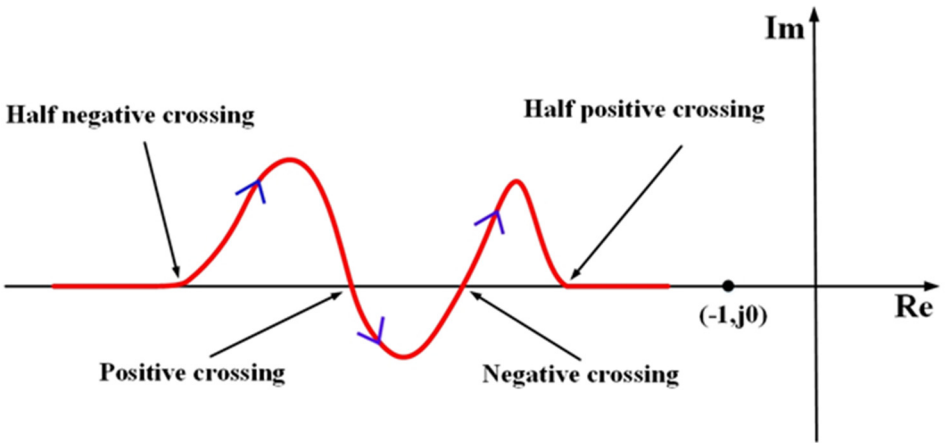

Figure 7. Overview of crossing manner (The arrow denotes the increasing ω).

4. Stability Analysis on MLSM with Gyroscopic Effect and Non-Collocated Structure

To apply the proposed extended inverse Nyquist stability criterion to the MLSM with gyroscopic effect and non-collocated structure, it is required that the open-loop transfer function of its equivalent SISO control system should be particularly discussed.

The open-loop transfer function of the equivalent SISO control system is:

$$G_{OL}(s) = \frac{\left[(J + mZ_sZ_F)s^2 - jJ_Z\Omega s + k_\theta\right]\left[K_Ds^2 + K_Ps + K_I\right]}{\left(Jms^4 - jmJ_Z\Omega s^3 + \left(mk_\theta - mk_sZ_F^2 - Jk_s\right)s^2 + jJ_Z\Omega k_s s - k_sk_\theta\right)s} \tag{23}$$

here, according to the definitions of transfer function [40] and Laplace transform [41], s is a complex variable generally written as $s = \sigma + j\omega$, where σ and ω represent the real part and the imaginary part, respectively. Then, by setting $G_{OL}(s) = 0$, zeros of the open-loop system get solved as:

$$s_{1,2} = \frac{-K_P \pm \sqrt{K_P^2 - 4K_DK_I}}{2K_D} \tag{24}$$

$$s_{3,4} = j\frac{J_Z\Omega \pm \sqrt{(J_Z\Omega)^2 + 4k_\theta(J + mZ_sZ_F)}}{2(J + mZ_sZ_F)} \tag{25}$$

Thereupon, the corresponding open-loop frequency response function can be derived as follows by making $\sigma = 0$:

$$G_{OL}(j\omega) = \frac{\left[-(J + mZ_sZ_F)\omega^2 + J_Z\Omega\omega + k_\theta\right]\left[-K_D\omega^2 + jK_P\omega + K_I\right]}{\left(Jm\omega^4 - mJ_Z\Omega\omega^3 - \left(mk_\theta - mk_sZ_F^2 - Jk_s\right)\omega^2 - J_Z\Omega k_s\omega - k_sk_\theta\right)j\omega} \quad (26)$$

More specifically, the frequency response functions of the MLSM system and the controller are given in (27) and (28), respectively:

$$G_{plant}(j\omega) = \frac{-(J + mZ_sZ_F)\omega^2 + J_Z\Omega\omega + k_\theta}{Jm\omega^4 - mJ_Z\Omega\omega^3 - \left(mk_\theta - mk_sZ_F^2 - Jk_s\right)\omega^2 - J_Z\Omega k_s\omega - k_sk_\theta} \quad (27)$$

$$G_{contr}(j\omega) = \frac{-K_D\omega^2 + jK_P\omega + K_I}{j\omega} \quad (28)$$

Since all of the three control parameters K_P, K_I and K_D always keep positive, $s_{1,2}$ definitely lie in the left half plane. As a result, there is no need for special handling when the inverse Nyquist curve is drawn. Nevertheless, this is not the case for $s_{3,4}$. Based on the value of $F = (J_Z\Omega)^2 + 4k_\theta(J + mZ_sZ_F)$, the zeros $s_{3,4}$ impact the inverse Nyquist plot of $G_{OL}(j\omega)$ in three distinct ways, which are explicitly presented in Table 1.

Table 1. Characteristics of the inverse Nyquist plot.

Condition	Zeros $s_{3,4}$	Characteristic of the Inverse Nyquist Plot
$F < 0$	Symmetry about the imaginary axis	Turn 180° clockwise from $\omega \to +\infty$ to $\omega \to -\infty$ with an infinite radius
$F = 0$	Double root on the imaginary axis	Turn 180° clockwise from $\omega \to +\infty$ to $\omega \to -\infty$ and 360° clockwise at $\omega_3 = \omega_4 = \frac{J_Z\Omega}{2(J+mZ_sZ_F)}$ with an infinite radius, respectively
$F > 0$	Two different roots on imaginary axis	Turn 180° clockwise from $\omega \to +\infty$ to $\omega \to -\infty$ and 180° clockwise at $\omega_{3,4} = \frac{J_Z\Omega \pm \sqrt{(J_Z\Omega)^2 + 4k_\theta(J+mZ_sZ_F)}}{2(J+mZ_sZ_F)}$ with an infinite radius, respectively

To summarize the distribution of zeros for $G_{OL}(s)$ according to Table 1, only when condition $F < 0$ is satisfied does one zero exist in the right half plane, while the remaining three zeros are located in the left half plane. Apart from this, there are two zeros in the left half plane and the other two are on the imaginary axis for both $F > 0$ and $F = 0$. So far, the inverse Nyquist stability criterion for the MLSM with gyroscopic effect and non-collocated structure can be given:

(1) When $(J_Z\Omega)^2 + 4k_\theta(J + mZ_sZ_F) < 0$, the sufficient and necessary condition for the absolute stability is that the inverse Nyquist curve of the open-loop transfer function G_{OL} encloses $(-1, j0)$ counterclockwise once.

(2) When $(J_Z\Omega)^2 + 4k_\theta(J + mZ_sZ_F) \geq 0$, the sufficient and necessary condition for the absolute stability is that the inverse Nyquist curve of the open-loop transfer function G_{OL} encircles $(-1, j0)$ zero times.

5. Simulation and Experimental Results

To verify the feasibility of the proposed methods, both simulation and experiments were implemented in this section. Figure 8a,b show the prototype MLSM and the corresponding rotor, of which the electromechanical specifications are presented in Table 2. In addition, electromagnetic structure of the MSLM has been presented in Figure 3 in this paper. The rotor consists of an aluminum-alloy counterweight (above) and a permanent

magnet (bellow) of the same inner diameter, outer diameter and thickness, i.e., their thicknesses equal 7 mm, respectively. Z_F can be set to different values by using counterweights of different thicknesses. Particularly, the laser displacement sensors are mounted on *z*-axis displacement platforms to adjust Z_s to different values. Then, we derived the parameters of Z_S, Z_F based on the following conditions: With the upper surface of the rotor taken as a reference, its center of gravity is calculated theoretically and the axial position of radial displacement sensors is estimated by the readings for *z*-axis displacement platforms. Besides, the equivalent application point of radial suspension force lies in the middle of confronting area between the rotor and stator. Four hall sensors are differentially mounted under the rotor in order to provide the information of speed and angular positions for control. Finally, a high-performance integrated controller executes the control algorithm with a sampling frequency of 10 kHz. Table 3 summarizes the corresponding physical and control parameters.

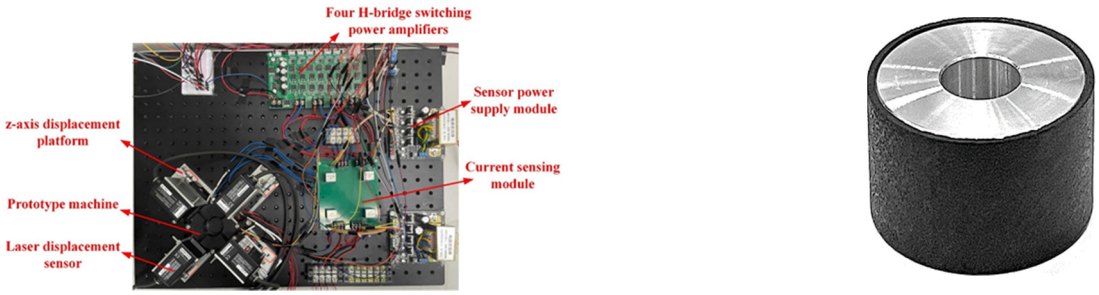

Figure 8. Picture of (**a**) the implemented MLSM system with the laser displacement sensors mounted on *z*-axis displacement platforms; (**b**) the rotor structure with $Z_F = -1.9$ mm.

Table 2. Electromechanical specifications of the illustrated MLSM.

Quantity	Value	Unit
Inner diameter of the rotor	11	mm
Outer diameter of the rotor	29	mm
Thickness of the rotor	14	mm
Inner diameter of the stator	36.5	mm
Outer diameter of the stator	61.5	mm
Height of the stator	54.26	mm
Phase of driving windings	2	//
Poles of driving windings	2	//
Phase of suspension windings	2	//
Poles of suspension windings	4	//

Table 3. System parameters relevant to the employed MLSM.

Parameter	Value	Parameter	Value
m	0.04 kg	k_θ	0.045 N·m/rad
J_Z	4.81×10^{-6} kg·m^2	K_P	10000 N/m
J	2.95×10^{-6} kg·m^2	K_I	5000 N/(m·s)
k_s	1389 N/m	K_D	20 N/(m/s)

Under the condition that Z_s is set to -2.2 mm and -0.3 mm, respectively, the inverse Nyquist curves are drawn from $\Omega = 300$ rad/s to $\Omega = 1200$ rad/s every 50 rad/s using the software MATLAB, which are based on the open-loop transfer function of the equivalent SISO control system by Equation (23). Here, we choose not to display the inverse Nyquist curves for all the speeds of $Z_s = -2.2$ mm, because they own similar trends to Figure 9 with the speeds bellow 600rad/s while the speeds over 600 rad/s result in the similarity

to Figure 10. In the cases of $Z_s = -0.3$ mm, only the inverse curves of $\Omega = 550$rad/s and $\Omega = 600$rad/s are presented in Figures 11 and 12 due to the same reason. Obviously, $F = (J_Z\Omega)^2 + 4k_\theta(J + mZ_sZ_F)$ is positive due to the positive Z_sZ_F, which satisfies the third case of Table 1. The inverse Nyquist curves turn 180° clockwise at the frequencies corresponding to the two different imaginary roots and from $\omega \to +\infty$ to $\omega \to -\infty$ with an infinite radius, separately, i.e., from A to A′, B to B′ and C to C′ in Figures 9–12. It can been seen that the inverse Nyquist curves circle $(-1, j0)$ counterclockwise zero times in Figures 9 and 12 but once in Figures 10 and 11.

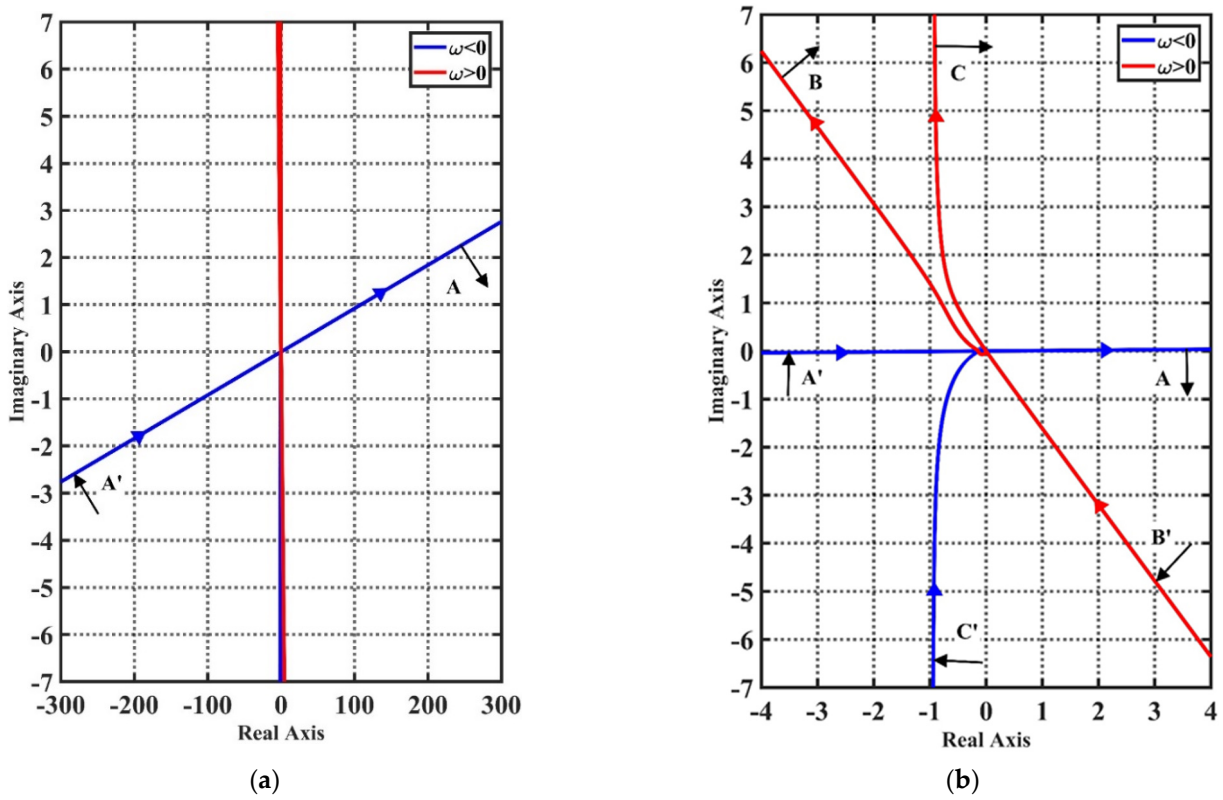

(**a**) (**b**)

Figure 9. Inverse Nyquist diagram for $\Omega = 500$ rad/s when $Z_s = -2.2$ mm. (**a**) Global; (**b**) Local. The inverse Nyquist curve turns 180° clockwise from A to A′, B to B′ and C to C′ with infinite radii. Thus, it circles $(-1, j0)$ zero times.

Given that the open-loop transfer function of the equivalent SISO control system holds no zeros on the right half-plane in all the cases researched, the sufficient and necessary condition for the absolute stability is that the corresponding inverse Nyquist curves of $G_{OL}(s)$ encircle $(-1, j0)$ zero times as demonstrated in Section 4. Specifically, the rotor can't operate stably until the spinning speed is below 600 rad/s when $Z_s = -2.2$ mm. Contrarily, if Z_s is set to -0.3 mm, the rotor is able to keep the stability of motion at a speed above 600 rad/s.

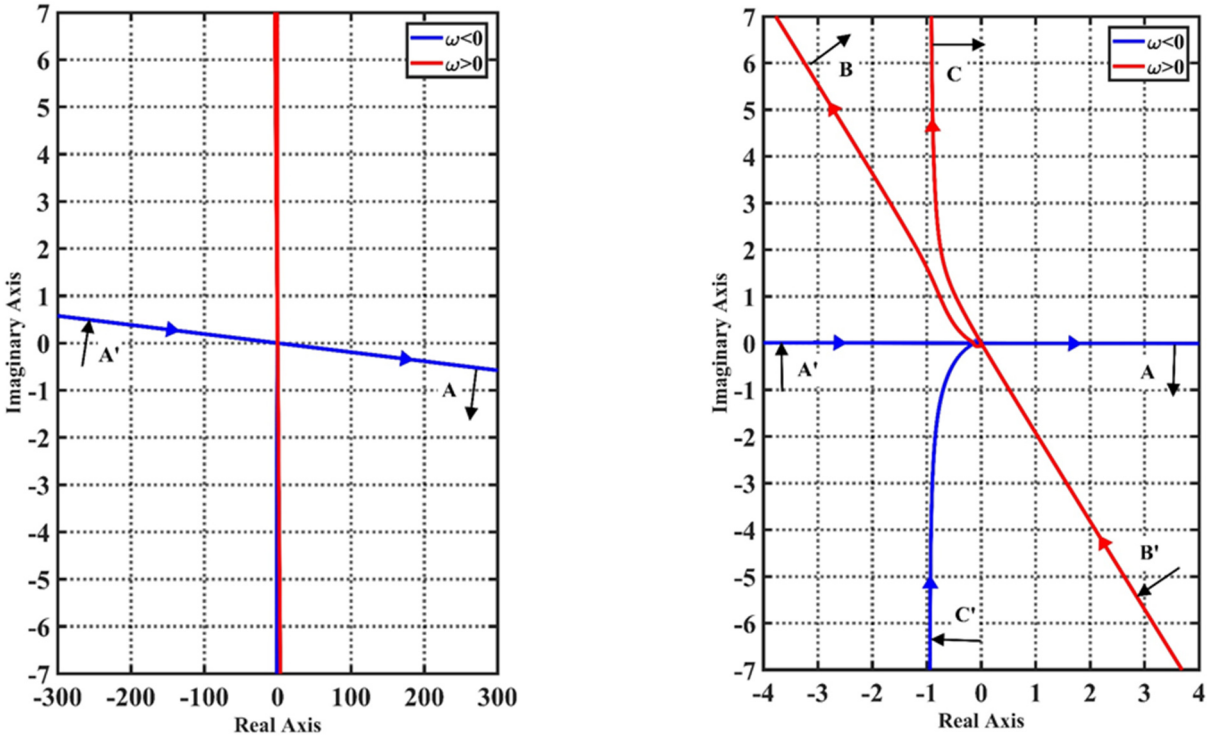

(**a**) (**b**)

Figure 10. Inverse Nyquist diagram for $\Omega = 600$ rad/s when $Z_s = -2.2$ mm. (**a**) Global; (**b**) Local. The inverse Nyquist curve turns 180° clockwise from A to A′, B to B′ and C to C′ with infinite radii. Thus, it circles $(-1, j0)$ once.

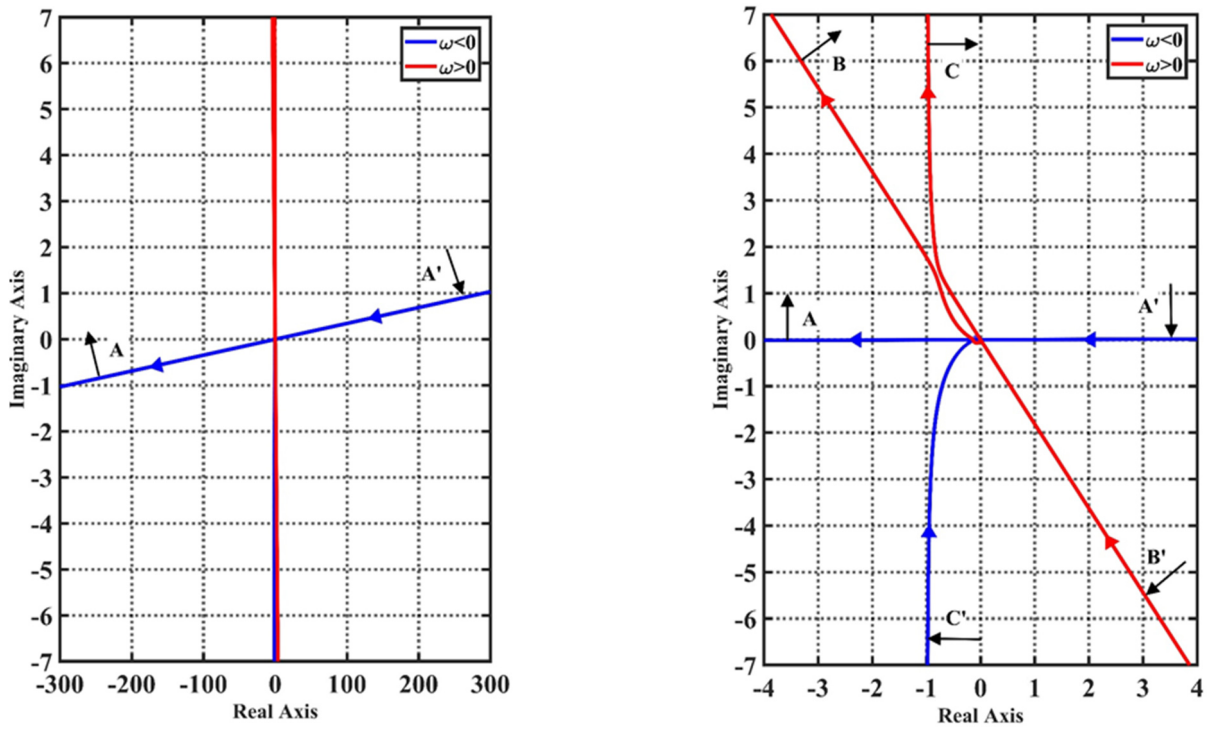

(**a**) (**b**)

Figure 11. Inverse Nyquist diagram for $\Omega = 550$ rad/s when $Z_s = -0.3$ mm. (**a**) Global; (**b**) Local. The inverse Nyquist curve turns 180° clockwise from A to A′, B to B′ and C to C′ with infinite radii. Thus, it circles $(-1, j0)$ once.

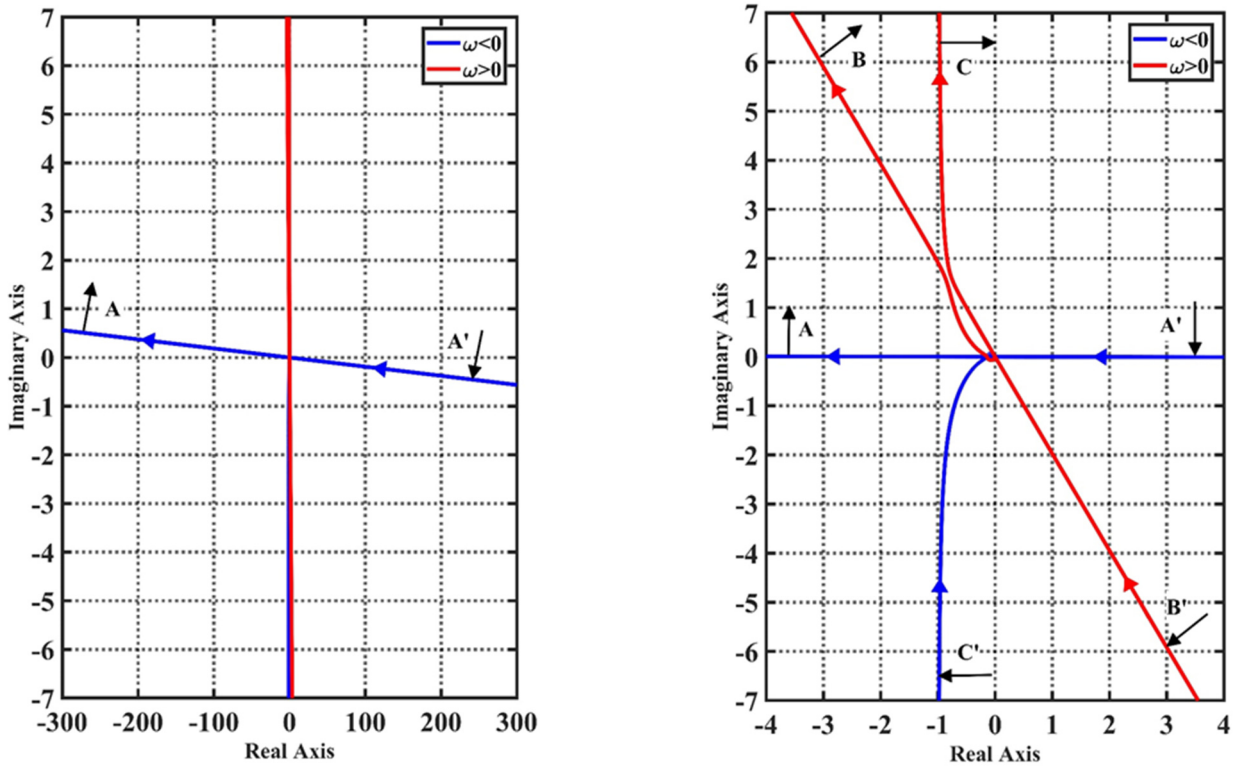

Figure 12. Inverse Nyquist diagram for $\Omega = 600$ rad/s when $Z_s = -0.3$ mm. (**a**) Global; (**b**) Local. The inverse Nyquist curve turns 180° clockwise from A to A′, B to B′ and C to C′ with infinite radii. Thus, it circles $(-1, j0)$ zero times.

Hereafter, corresponding experiments were implemented to prove the effectiveness of the simulation results. Figure 13 shows the experiment results at $Z_s = -2.2$ mm, and the rotor is speeded up to 300 rad/s after start-up. It is indicated that the rotor can operate without collision and the maximum radial vibration displacements are less than 400 μm. As the rotary speed increases successively, radial displacements fluctuate less. Nevertheless, once the speed reaches 600 rad/s, radial vibration displacements begin to enlarge over time and then the rotor collides with the stator (The rotor will collide with the stator if radial vibration displacements surpass 500 μm). The above phenomenon accords with the result deduced by the inverse Nyquist stability criterion that the rotor loses its stability with a speed above 600 rad/s as $Z_s = -2.2$ mm. Afterwards, Z_s is set to -0.3 mm by adjusting z-axis displacement platforms. Progressively, the rotor speeds up to 1200 rad/s and subsequently slows down to 550 rad/s. Figure 14 presents the whole decelerating process. Obviously, the rotor suspends and rotates stably with radial vibration displacements no more than 250 μm above 600 rad/s. However, the rotor runs into the stator frequently when it slows down to 550 rad/s. In this situation, the rotor can keep stable only when the speed exceeds 600 rad/s, corresponding to the conclusion drawn for $Z_s = -0.3$mm by the inverse Nyquist stability criterion. To summarize, the experimental results are consistent with the simulation results.

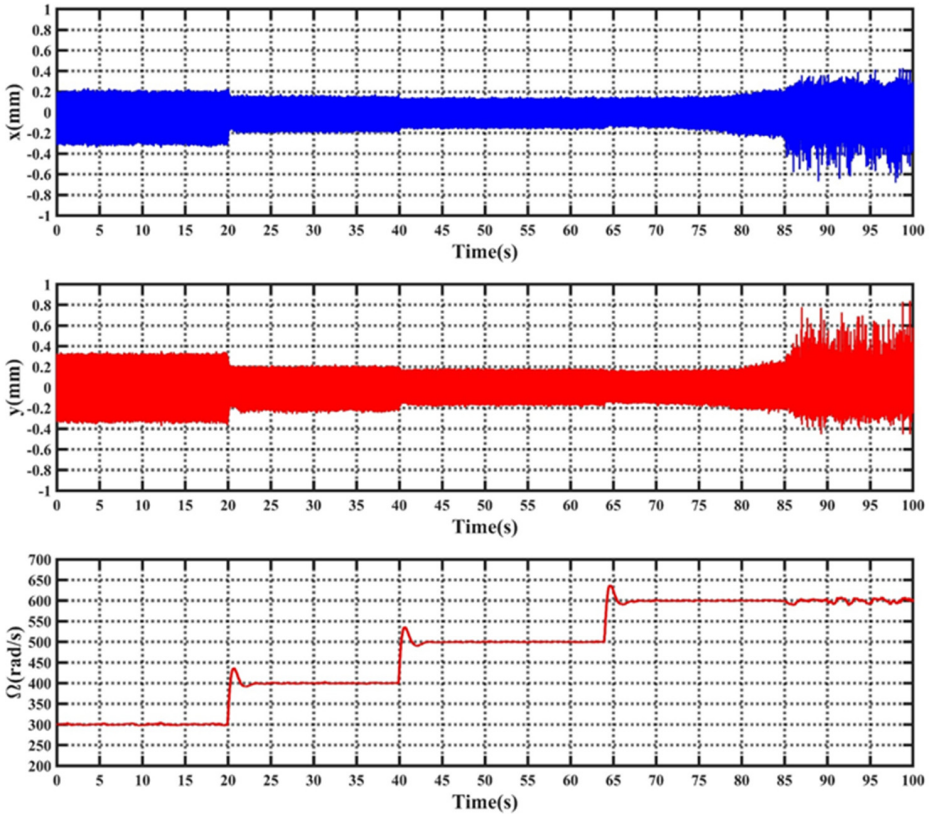

Figure 13. Experimental results: when $Z_s = -2.2$ mm, the radial vibration displacements in *x*- and *y*-directions are presented corresponding to different rotary speeds.

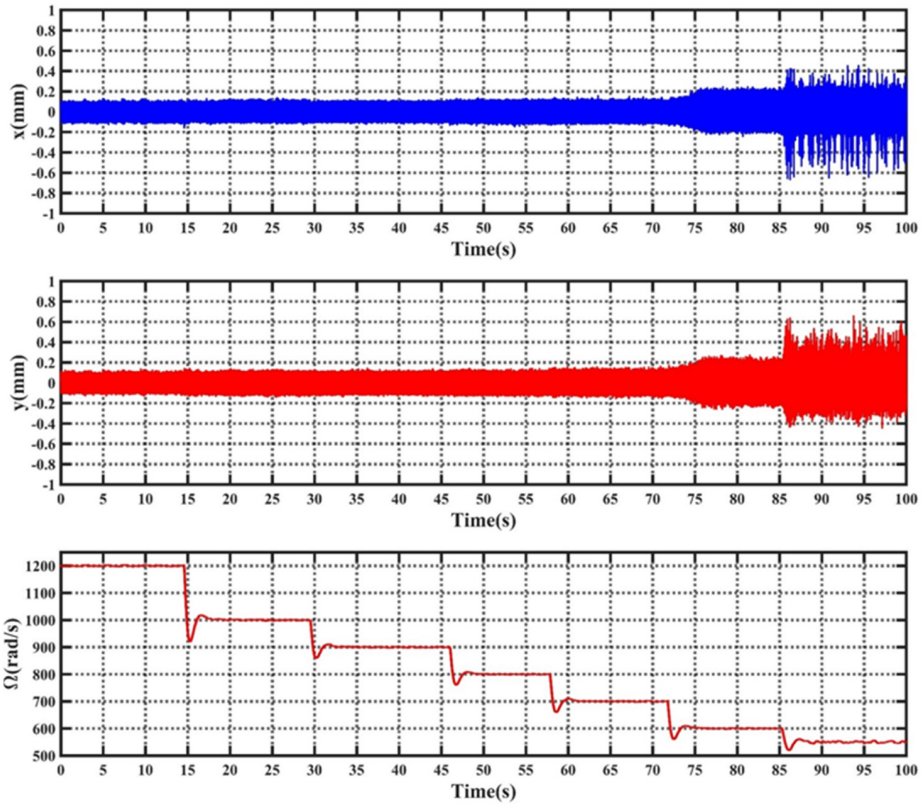

Figure 14. Experimental results: when $Z_s = -0.3$ mm, the radial vibration displacements in *x*- and *y*-directions are presented corresponding to different rotary speeds.

6. Conclusions

In this paper we propose a method of modelling and a stability analysis for a magnetically levitated slice motor (MLSM) with simultaneous gyroscopic effect and non-collocated structure, which was characterized by a strongly coupled multiple-input and multiple-output (MIMO) model. A block diagram indicated that radial translational displacements, tilting displacements and spin velocity interfered for the rotors of the MLSM, where the center of gravity of rotor, the axial position of radial displacement sensors, and the equivalent application point of active radial suspension force were not collocated. A novel MIMO rotor dynamics closed-loop model was set up to describe the strongly coupled system and then was converted into an equivalent single-input and single-output (SISO) feedback control system with complex coefficients. With respect to the above-mentioned SISO system, the extended inverse Nyquist stability criterion in the complex domain offered the way to deduce the sufficient and necessary condition for its absolute stability. Eventually, simulation and experiments were conducted on a MLSM prototype operating with different spin velocities and different axial positions of radial displacement sensors, which confirmed that the proposed method of modelling and stability analysis was valid to analyze such MLSM systems.

Author Contributions: Conceptualization, L.L.; methodology, L.L., Y.Y., L.H., X.R., R.S. and X.F.; validation, L.L.; writing—original draft preparation, L.L.; writing—review and editing, L.H., X.R., R.S. and X.F.; supervision, X.F., X.R., R.S. and L.H.; project administration, X.F. All authors have read and agreed to the published version of the manuscript.

Funding: This work was supported by the Natural Science Foundation of Zhejiang Province (No. LY19E050015), the National Natural Science Foundation of China (No. 52075475), and the Science Fund for Creative Research Groups of National Natural Science Foundation of China (No. 51821093).

Conflicts of Interest: The authors declare no conflict of interest.

Nomenclature

MLSM	Magnetically levitated slice motor.
MIMO	Multiple-input and multiple-output.
SISO	Single-input and single-out.
N_{Bd}, N_{Bq}, N_{dd}, N_{dq}	Suspension coils and driving coils.
α, β, γ	Inclinations of rotor about *x*-, *y*-, and *z*-axes.
Ω	Spin velocity.
M	Mass of the rotor.
J_Z	Moment of inertia of the rotor about *Z*-axis.
J	Moment of inertia of the rotor about X- and Y-axes.
k_s	Radial stiffness in x-and y-directions.
k_θ	Tilting stiffness in x-and y-directions.
d_x, d_y	Total disturbance forces in x-and y-directions.
T_α, T_β	Total disturbance moments in x-and y-directions.
S	Axial position of radial displacement sensors.
F	Equivalent application point of radial suspension force.
N	Center of gravity of rotor.
Z_s	Distance of S with respect to N.
Z_F	Distance of F with respect to N.
K_p, K_I, K_D	Parameters of the radial translational controllers.

References

1. Warberger, B.; Kaelin, R.; Nussbaumer, T.; Kolar, J.W. 50-/2500-W Bearingless Motor for High-Purity Pharmaceutical Mixing. *IEEE Trans. Ind. Electron.* **2012**, *59*, 2236–2247. [CrossRef]
2. Li, Q.N.; Boesch, P.; Haefliger, M.; Kolar, J.W.; Xu, D.H. Basic characteristics of a 4kW permanent-magnet type bearingless slice motor for centrifugal pump system. In Proceedings of the 2008 International Conference on Electrical Machines and Systems, Wuhan, China, 17–20 October 2008; pp. 3037–3042.

3. Press Release IBM. Chartered, Infineon and Samsung Announce Process and Design Readiness for Silicon Circuits on 45 nm Low-Power Technology. Available online: https://www.design-reuse.com/news/14108/ibm-chartered-infineon-samsung-process-design-readiness-silicon-circuits-45nm-power-technology.html (accessed on 13 September 2021).
4. Neff, M.; Barletta, N.; Schöb, R. Bearingless Centrifugal Pump for Highly Pure Chemicals. In Proceedings of the 8th International Symposium on Magnetic Bearing, Mito, Japan, 26–28 August 2002.
5. Bu, W.S.; Huang, S.H.; Wan, S.M.; Liu, W.S. General Analytical Models of Inductance Matrices of Four-Pole Bearingless Motors with Two-Pole Controlling Windings. *IEEE Trans. Magn.* **2009**, *45*, 3316–3321. [CrossRef]
6. Weinreb, B.S. A novel Magnetically Levitated Interior Permanent Magnet Slice Motor. Master's Thesis, Massachusetts Institute of Technology, Cambridge, MA, USA, 2020.
7. Zhang, S.R.; Fang, L.L. Direct Control of Radial Displacement for Bearingless Permanent-Magnet-Type Synchronous Motors. *IEEE Trans. Ind. Electron.* **2009**, *56*, 542–552. [CrossRef]
8. Mitterhofer, H. Towards High-Speed Bearingless Disk Drives. Ph.D. Thesis, Johannes Kepler University Linz, Linz, Austria, 2017.
9. Ahrens, M.; Kucera, L.; Larsonneur, R. Performance of a magnetically suspended flywheel energy storage device. *IEEE Trans. Control Syst. Technol.* **1996**, *4*, 494–502. [CrossRef]
10. Sun, M.L.; Zheng, S.Q.; Wang, K.; Le, Y. Filter Cross-Feedback Control for Nutation Mode of Asymmetric Rotors with Gyroscopic Effects. *IEEE ASME Trans. Mechatron.* **2020**, *25*, 248–258. [CrossRef]
11. Ahrens, M.; Kucera, L. Cross Feedback Control of a Magnetic Bearing System: Controller Design Considering Gyroscopic Effects. In Proceedings of the 3th International Symposium on Magnetic Suspension Technology, Tallahassee, FL, USA, 13–15 December 1995.
12. Karutz, P.; Nussbaumer, T.; Gruber, W.; Kolar, J.W. Novel Magnetically Levitated Two-Level Motor. *IEEE ASME Trans Mechatron.* **2008**, *13*, 658–668. [CrossRef]
13. Masuzawa, T.; Kita, T.; Okada, Y. An ultradurable and compact rotary blood pump with a magnetically suspended impeller in the radial direction. *Artif. Organs* **2015**, *25*, 395–399. [CrossRef] [PubMed]
14. Bartholet, M.T.; Nussbaumer, T.; Silber, S.; Kolar, J.W. Comparative Evaluation of Polyphase Bearingless Slice Motors for Fluid-Handling Applications. *IEEE Trans. Ind. Appl.* **2009**, *45*, 1821–1830. [CrossRef]
15. Sugimoto, H.; Chiba, A. Stability Consideration of Magnetic Suspension in Two-Axis Actively Positioned Bearingless Motor with Collocation Problem. *IEEE Trans. Ind. Appl.* **2014**, *50*, 338–345. [CrossRef]
16. Tang, J.Q.; Zhao, S.P.; Wang, Y.; Wang, K. High-speed Rotor's Mechanical Design and Stable Suspension Based on Inertia-ratio for Gyroscopic Effect Suppression. *Int. J. Control Autom.* **2018**, *16*, 1577–1591. [CrossRef]
17. Schweitze, G.; Maslen, E. *Magnetic Bearings-Theory, Design, and Application to Rotating Machinery*; Springer: Berlin/Heidelberg, Germany, 2009; pp. 168–179.
18. Fang, J.C.; Ren, Y.; Fan, Y.H. Nutation and Precession Stability Criterion of Magnetically Suspended Rigid Rotors with Gyroscopic Effects Based on Positive and Negative Frequency Characteristics. *IEEE Trans. Ind. Electron.* **2013**, *61*, 2003–2014. [CrossRef]
19. Wei, J.B.; Liu, K.; Radice, G. Study on stability and rotating speed stable region of magnetically suspended rigid rotors using extended Nyquist criterion and gain-stable region theory. *ISA Trans.* **2016**, *66*, 154–163. [CrossRef] [PubMed]
20. Sugimoto, H.; Shimura, I.; Chiba, A. A novel simplified structure for single-drive bearingless motor. In Proceedings of the 2016 IEEE Energy Conversion Congress and Exposition (ECCE), Milwaukee, WI, USA, 18–22 September 2016; pp. 1–7. [CrossRef]
21. Sugimoto, H.; Chiba, A. Experimental Results Passing Through Critical Speeds of Radial and Tilting Motions in a One-Axis Actively Positioned Single-Drive Bearingless Motor. In Proceedings of the 2018 IEEE Energy Conversion Congress and Exposition (ECCE), Portland, OR, USA, 23–27 September 2018; pp. 4392–4397. [CrossRef]
22. Sugimoto, H.; Miyoshi, M.; Chiba, A. Low speed test in two-axis actively positioned bearingless machines with non-collocated structure for wind power applications. In Proceedings of the 2015 IEEE Energy Conversion Congress and Exposition (ECCE), Montreal, QC, Canada, 20–24 September 2015; pp. 799–804. [CrossRef]
23. Sun, X.D.; Chen, L.; Yang, Z.B. Overview of Bearingless Permanent-Magnet Synchronous Motors. *IEEE Trans. Ind. Electron.* **2013**, *60*, 5528–5538. [CrossRef]
24. Raggl, K.; Kolar, J.W. Comparison of Winding Concepts for Bearingless Pumps. In Proceedings of the 7th International Conference on Power Electronics, Daegu, Korea, 22–26 October 2007; pp. 1013–1020. [CrossRef]
25. Ooshima, M.; Chiba, A.; Fukao, T. Design and Analysis of Permanent Magnet-Type Bearingless Motors. *IEEE Trans. Ind. Electron.* **1996**, *43*, 292–299. [CrossRef]
26. Mamat, N.; Karim, K.A.; Ibrahim, Z. Bearingless Permanent Magnet Synchronous Motor using Independent Control. *Int. J. Power Electron. Drive Syst.* **2015**, *6*, 233–241. [CrossRef]
27. Zhang, W.; Zhu, H.Q.; Xu, Y.; Wu, M.Y. Direct Control of Bearingless Permanent Magnet Slice Motor Based on Active Disturbance Rejection Control. *IEEE Trans. Appl. Supercon.* **2020**, *30*, 1–5. [CrossRef]
28. Mitterhofer, M.; Amrhein, W. Design aspects and test results of a high speed bearingless drive. In Proceedings of the 2011 IEEE Ninth International Conference on Power Electronics and Drive Systems, Singapore, 5–8 December 2011; pp. 705–710. [CrossRef]
29. Zhu, H.Q.; Li, F.Y. Optimization Design of Bearingless Permanent-Magnet Slice Motor. *IEEE Trans. Appl. Supercon.* **2016**, *26*, 1–4. [CrossRef]
30. Michioka, C.; Sakamoto, T.; Ichikawa, O.; Chiba, A.; Fukao, T. A decoupling control method of reluctance-type bearingless motors considering magnetic saturation. *IEEE Trans. Ind. Appl.* **1996**, *32*, 1204–1210. [CrossRef]

31. Bouzidi, R.; Van, A.L. *Lagrangian Mechanics: An Advanced Analytical Approach*; Wiley-ISTE: Hoboken, NJ, USA; London, UK, 2019; pp. 111–129.
32. Bösch, P.N. Lagerlose Scheibenläufermotoren höherer Leistung. Ph.D. Thesis, ETH Zurich, Zurich, Switzerland, 2004.
33. Liu, C.; Liu, G. Equivalent Damping Control of Radial Twist Motion for Permanent Magnetic Bearings Based on Radial Position Variation. *IEEE Trans. Ind. Electron.* **2015**, *62*, 6417–6427. [CrossRef]
34. Troeng, O.; Bernhardsson, B.; Rivetta, C. Complex-coefficient systems in control. In Proceedings of the 2017 American Control Conference (ACC), Seattle, WA, USA, 24–26 May 2017; pp. 1721–1727. [CrossRef]
35. Zhang, S.C.; Xia, Y.S. Solving Nonlinear Optimization Problems of Real Functions in Complex Variables by Complex-Valued Iterative Methods. *IEEE Trans. Cybern.* **2018**, *48*, 277–287. [CrossRef]
36. Ahlfors, L. *Complex Analysis*; McGraw-Hill: New York, NY, USA, 1979.
37. Garcia-Sanz, M. The Nyquist stability criterion in the Nichols chart. *Int. J. Robust Nonlinear Control* **2016**, *26*, 2643–2651. [CrossRef]
38. Fang, B. Computation of stabilizing PID gain regions based on the inverse Nyquist plot. *J. Process Control* **2010**, *20*, 1183–1187. [CrossRef]
39. Wen, B.; Boroyevich, D.; Burgos, R. Inverse Nyquist Stability Criterion for Grid-Tied Inverters. *IEEE Trans. Power Electron.* **2016**, *32*, 1548–1556. [CrossRef]
40. Ogata, K. *Modern Control Engineering*, 5th ed.; Prentice-Hall: Englewood Cliffs, NJ, USA, 2010; pp. 398–462.
41. Oppenheim, A.V.; Nawab, S.H.; Willsky, A.S. *Signals and Systems*, 2nd ed.; Prentice-Hall: Englewood Cliffs, NJ, USA, 1997; pp. 461–485.